Mol. Cryst. Liq. Cryst., Vol. 477, pp. 23/[517]–41/[535], 2007

ISSN: 1542-1406 print/1563-5287 online
DOI: 10.1080/15421400701683956

Confocal Microscopy of Director Structures in Strongly Confined and Composite Systems

Ivan I. Smalyukh
Chemical Physics Interdisciplinary Program and the Liquid Crystal Institute, Kent State University, Kent, OH, USA

We review approaches for simultaneous imaging of three-dimensional director structures and component distributions in composite materials using fluorescence confocal polarizing microscopy. To study dynamic processes in these systems, we use the Nipkow-disk microscope in which the confocal images are obtained within milliseconds. The visualized director fields, free-standing film profiles, and ordered colloidal structures provide insights into the physics phenomena ranging from elasticity-mediated self-organization to anchoring-assisted levitation and dynamics of micron-sized spheres.

Keywords: colloid; defect; fluorescence confocal polarizing microscopy; free-standing film; liquid crystal; surface anchoring

1. INTRODUCTION

Orientational order is an important property of liquid crystals (LCs) and other materials [1,2]. Molecular interactions responsible for this ordering are rather weak, so that the spatial structures of the LC director $\hat{n}(\vec{r})$ can be modified by many factors including surface treatment, temperature changes, flow, colloidal inclusions, magnetic and electric fields, etc [1,2]. Non-destructive imaging of the three-dimensional (3-D) spatial patterns of $\hat{n}(\vec{r})$ and component distributions in composite LC materials is important for both applied and fundamental

We acknowledge the support of the Institute for Complex Adaptive Matter (ICAM) and International Institute for Complex Adaptive Matter (I2CAM), the National Science Foundation, Grant DMR# 0645461 and thank A. Kachynski, O. Lavrentovich, M. Nobili, B. Senyuk, and S. Shiyanovskii for discussions and collaborations.

Address correspondence to Ivan I. Smalyukh, Department of Physics and Liquid Crystal Materials Research Center, University of Colorado at Boulder, Boulder, CO 80309, USA. E-mail: Ivan.smalyukh@colorado.edu

research. Fluorescence confocal microscopy (FCM) is broadly used to study the composite systems in 3-D [3,4] and employs coordinate-dependent dye concentrations (dyes segregate into different components) [4]. Recently, the new class of the detectors allowed researches to develop the Nipkow-disc scanning microscope (with numerous pinholes in the spinning disc) capable of FCM imaging at rates $\sim$1000 frames per second [5]. On the other hand, by using (a) fluorescent dye composed of anisometric molecules and (b) polarized excitation and fluorescence detection, one can transform the regular FCM into a technique that visualizes 3-D director fields, called Fluorescence Confocal Polarizing Microscopy (FCPM) [6]. In this approach, the absorption/fluorescence transition dipoles of the used dye molecules homogeneously distribute in the LC sample and follow $\hat{n}(\vec{r})$. When confocal imaging is performed with a controlled polarization state, the technique visualizes the 3-D pattern of $\hat{n}(\vec{r})$. The director structures are reconstructed based on multiple confocal images obtained for different FCPM polarization states and different sample cross-sections. The technique has been used to study electro-optic effects in nematic LCs [6–8], focal conic domains in smectics [6,8], defects [9,10] and layers undulations [11] in cholesterics, director distortions around beads [12–13], orthogonal director fields in biaxial LCs [14], and the ordered structures in anisotropic colloidal systems [15].

In this article, we review approaches for the simultaneous study of static and dynamic $\hat{n}(\vec{r})$ in composite and confined materials [6–18]. Fluorescence dye molecules in these composite systems can follow the LC director and also can segregate into different components. The texture analysis is complicated by the non-homogeneity of dye distributions and the finite diffraction-limited FCPM resolution. We therefore use multiple dye labeling and spectral separation of fluorescent signals from specially-selected dyes as well as a comparison with computer simulations. This allows one to decipher $\hat{n}(\vec{r})$ in confined LCs, free-standing films, phase-separated systems and colloidal suspensions, providing also information on the spatial location of different components. Finally, FCPM and other non-invasive imaging techniques, such as coherent anti-Stokes Raman scattering microscopy, are discussed from the standpoint of applications in the study of composite LC systems.

2. EXPERIMENT

2.1. Experimental Setups

Figure 1a shows the FCPM set up based on an Olympus Fluoview BX-50 confocal microscope. An achromatic linear polarization rotator

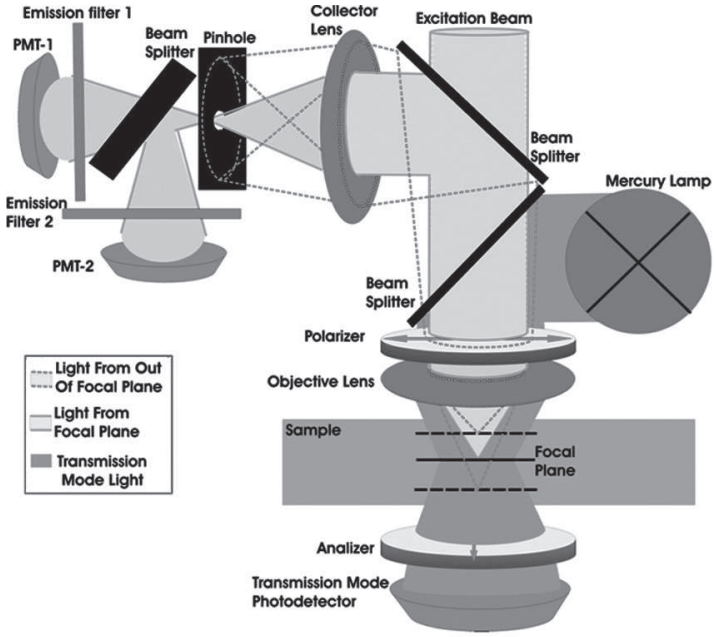

(a)

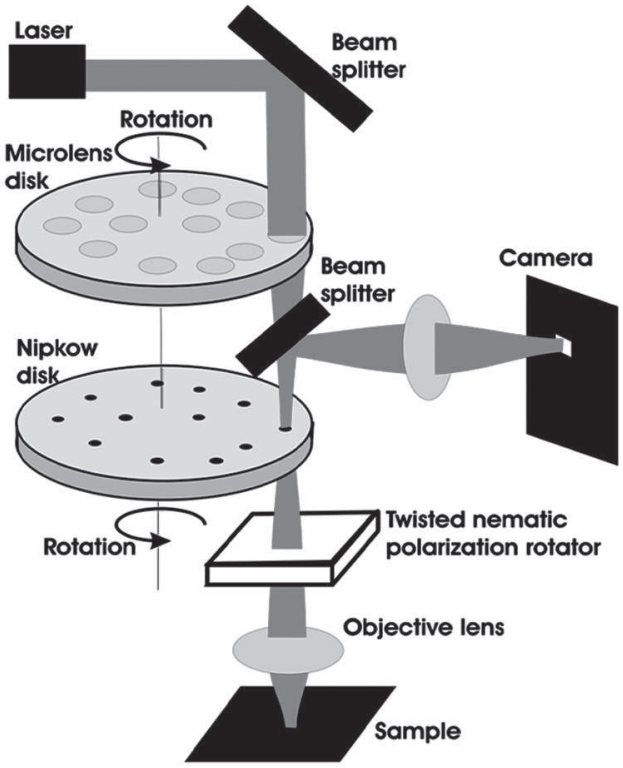

(b)

FIGURE 1 (a) Two-channel FCPM and (b) fast FCPM based on a Nipkow-disk confocal microscope.

is used to control the polarization of both excitation and detected fluorescent light. Laser beam power is $<1\,\mathrm{mW}$ to avoid laser-induced director reorientation [16] and the effects of optical gradient forces on the structures [17]. The excitation beam (488 nm Ar-laser, or 568 nm Kr-laser) is focused by an objective into a small ($<1\,\mu\mathrm{m}^3$) volume in the sample. Fluorescent light from this volume is detected by a photomultiplier tube. For dyes excited by the Ar-laser, the emission light is detected in the spectral region 510–550 nm [6,18,19] selected by interference filters (channel #1). For dyes excited by the Kr-laser, the emission detection is performed in the range 580–650 nm (channel #2). A pinhole (in a focal plane next to the detector) discriminates against the regions above and below the selected volume in the studied sample, Figure 1a. The pinhole size is adjusted depending on objective's magnification and numerical aperture (NA); we use an immersion-oil objective (60X, NA = 1.4) and a dry objective (40X, NA = 0.6). A focused beam scans a sample in horizontal planes at different fixed depths. Coordinate-dependent fluorescence intensity data are stored in the computer memory and then used to compose the sample's cross-sections and to reconstruct a 3-D image.

The fast confocal imaging system, Figure 1b, employs a rotating Nipkow disk with a pattern of pinholes. This disk is rotated by an electrical motor and often supplemented by a coaxial mechanically-coupled disk with micro-lenses. The sample is scanned by thousands of beams at once, and imaging is faster by orders of magnitude as compared to a conventional confocal microscope. The Fast FCPM set up, Figure 1b, is integrated with a Nikon microscope Eclipse E-600. The vertical refocusing is performed by a piezo stepper drive (obtained from PI Piezo) capable of an accurate (50 nm) vertical position setting. The imaging speed can be 100–1000 frames per second, depending on such factors as integration time of the fluorescence signal, size of the scanned area, and characteristics of the CCD camera. Thus, the Nipkow-disk-type confocal microscope can probe dynamic processes.

2.2. Fluorescent Probes

The used fluorescent dyes (Fig. 2) are doped at tiny concentrations (usually $\sim 0.01\,\mathrm{Wt.\%}$, sufficient to produce a strong fluorescence signal for the director reconstruction) and do not alter the LC properties. The dye's order parameter in LC hosts needs to be large for the director imaging. Dyes with low order parameters (whose fluorescence signal is polarization-independent) are useful to study component distributions in the composite materials. For the study of heterogeneous systems one often needs to use multiple dyes specially selected for

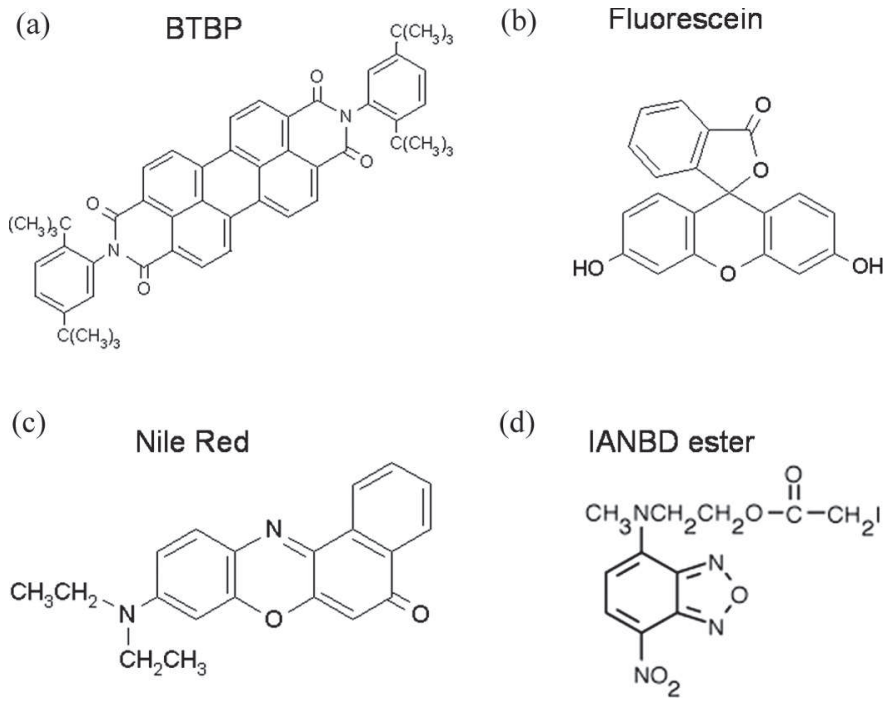

FIGURE 2 Chemical structures of the used fluorescent dyes: (a) *N,N′*-Bis(2,5-di-*tert*-butylphenyl)-3,4,9,10perylenedicarboximide (BTBP); (b) Fluorescein; (c) Nile Red; (d) *N*-((2-(iodoacetoxy)ethyl)-*N*-methyl)amino-7-nitrobenz-2-oxa-1,3-diazole (IANBD ester).

different components, as discussed below for specific examples. Dyes used for director imaging, such as the n,n′-bis(2,5-di-tert-butylphenyl)-3,4,9,10-perylenedicarb-oximide (BTBP, Fig. 2a), have relatively short fluorescence lifetime ($\tau_f = (3.7 - 3.9)$ns for BTBP [19]) which is smaller than the characteristic time of rotational diffusion $\tau_D \approx 10$ ns in LCs. Therefore, molecule orientations during absorption and emission are assumed to be the same [6,7]. The translational diffusion coefficient for most dye molecules in LCs is $D \sim 10^{-10}\,\mathrm{m}^2/\mathrm{s}$. Therefore, to diffuse a distance $L = 1\,\mu$m, the dye molecule would need time $t \approx L^2/D \approx 10$ ms, which is much larger than the time during which the fluorescent light is emitted. Therefore, the dye molecule emits within the same diffraction-limited volume in which it was excited.

2.3. Polarization Rotator for FCPM

In principle, the FCPM polarization can be changed by rotating a polarizer in the common path of excitation and emission light (Figure 1). However, this approach has disadvantages: (a) the excitation intensity

varies with polarizer rotation due to the initial partially-polarized state of excitation light; (b) mechanical rotation is slow and allows one to image only stationary $\hat{n}(\vec{r})$. To control polarization state of spectrally-separated excitation and fluorescence light, we equipped the microscope with an achromatic polarization rotator based on a twisted nematic (TN) cell. The achromatic polarization switching in the TN cell is achieved by satisfying the Mauguin condition $p\Delta n/(2\lambda) = 2d\Delta n/\lambda >> 1$ (where d is the cell thickness and $p = d/4$ is the pitch of twist, i.e. the distance over which director twists for 2π) [1,2]. In the Mauguin regime, the polarization plane is rotated nearly exactly by the angle of twist in the TN cell as light polarization closely follows the twist. We use a high-birefringence LC [18] in order to satisfy the above conditions for the thin $(4-5)\mu m$ cells, so that switching is fast ($\sim 5\,ms$). By applying an electric field across the cell, one switches the structure from twisted to vertical state that does not alter the light's polarization state; this effect allows one to switch the FCPM polarization between two orthogonal directions. This polarization rotator combines advantages of (a) wavelength-independent (within the visible spectral range) characteristics, (b) low-voltage ($< 10\,V$) driving scheme, and (c) fast switching between the two orthogonal polarization states. Therefore, in addition to its conventional capabilities, the Nipkow-disk-type FCPM with the polarization rotator can probe the director dynamics.

2.4. Basic Principles of FCPM Imaging

When a nematic LC is doped with a fluorescent dye such as BTBP with the transition dipoles of both excitation and fluorescence along the long molecule's axis, Figure 2a, the transition dipoles follow the director [6]. The absorption efficiency of a linearly polarized laser light is determined by the angle between the polarization $\widehat{P}$ and the dye's absorption transition dipole, usually as $\propto \cos^2\alpha$, where α is the angle between the dipole and $\widehat{P}$ [6,8]. When the excited dye emits, the fluorescence signal is rooted through the very same objective and a polarization rotator in the reflective-mode FCPM, Figure 1. The intensity of detected fluorescence light depends on the angle between $\widehat{P}$ and the emission transition dipole of the dye, usually as $\propto \cos^2\alpha$ [6–8]. The FCPM fluorescence intensity is then $I \propto \cos^4\alpha$. These FCPM imaging principles allow one to decipher the LC director structures in 3-D [6–8].

In confined samples of thickness $(1-10)\mu m$, director distortions also have micrometer lengths. Therefore, an important issue is the imaging resolution. In an isotropic medium, the confocal microscopy

resolution that can be achieved using an immersion oil 60X objective with NA = 1.4 is $\sim 0.2\,\mu m$ in the lateral plane perpendicular to the microscope's axis and $\sim 0.6\,\mu m$ along the axis [3,4]. However, resolution is usually worse in birefringent media such as LCs, in which the tight beam focusing is difficult and accompanied with various aberrations. Since the spatial defocusing of the ordinary and extraordinary modes at depth of scanning z is $\propto \Delta n \cdot z$ [7,8], one can use LCs with a low birefringence Δn to reduce the aberrations. The finite FCPM resolution has to be accounted for in the analysis of fluorescence textures with typical length scales of the order of micrometers.

3. RESULTS AND DISCUSSION

3.1. Field-Induced Periodic Structures in Cholesteric LCs

In thin cholesteric cells, LC elasticity, chirality, surface anchoring, and coupling to external fields can result in a rich variety of structures with spatial features in the range of microns. The finite diffraction-limited resolution ($\approx 1\,\mu m$) results in "blurring" of the micron-sized features of FCPM images and has to be accounted for [6–8]. To demonstrate this, we use a planar cholesteric slab ($< 10\,\mu m$) prepared between transparent electro-conductive plates with rubbed polyimide PI2555 alignment layers. The cholesteric LC (a mixture of nematic host ZLI-3412 and a chiral agent CB15, both from EM Chemicals) is further doped with BTBP, Figure 2a (Molecular Probes). BTBP contains no ionic groups and is therefore suitable for the director imaging under applied electric fields that do not effect dye spatial distribution. When excited by an Ar-laser at 488 nm, BTBP shows maximum absorption and fluorescence for linear FCPM polarization along the long molecular axis and minimum for the orthogonal case, which is used for the LC director imaging. At small voltages, the cholesteric planar structure remains uniform (Fig. 3b,c). The FCPM vertical cross-sections obtained for orthogonal polarizations (Fig. 3b,c) show that the two different Grandjean zones with π and 2π twist are separated by a pair of $\tau^{-1/2}$ and $\lambda^{1/2}$ disclinations [9,10]. Since ZLI-3412 has a positive dielectric anisotropy $\Delta\varepsilon = 3.4$, the applied field tends to reorient the director vertically. At voltages $> 10\,V$, the structure is completely unwound (with the exception of thin layers at bounding plates) and the director is along the cell normal. At intermediate voltages such as 2.1 V, one observes in-plane periodic patterns with the stripe orientation either along the rubbing direction or perpendicular to it, Figure 3a. The structure (Fig. 3d,e) resembles the Helfrich-Hurault undulations observed in multi-layered ($d/p >> 1$) cholesteric samples under applied fields [1,2,11].

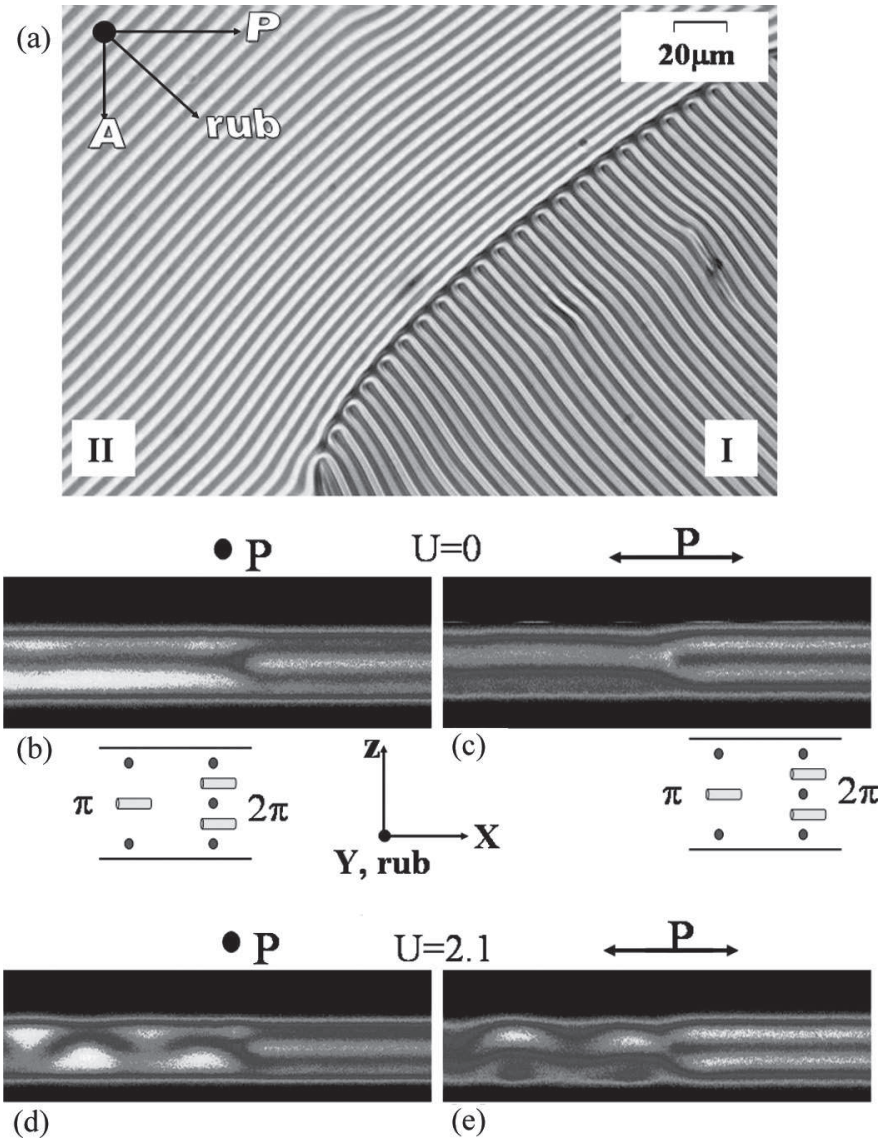

FIGURE 3 (a) Polarizing microscopy texture of field-induced (I) parallel and (II) perpendicular stripes in a cholesteric cell. Arrows show the rubbing direction and crossed polarizers. (b-e) FCPM textures of the cell's vertical cross-section in the region between the π- and 2π-Grandjean zones at (b,c) no applied field and (d,e) at applied 2.1 V, 1 kHz.

Figure 4 shows a periodic structure of dark/bright stripes being parallel to the rubbing direction in a cell of thickness over pitch ratio $d/p \approx 0.7$. At no applied voltage, this part of the cell exhibits a planar cholesteric texture with π-twisted $\hat{n}(\vec{r})$ matching planar boundary conditions at substrates. FCPM textures in Figure 4c,d are obtained for two orthogonal polarizations. The computer-simulated director structure in Figure 4b and the respective FCPM texture in Figure 4e (see Ref. [7] for details on computer simulations) closely match to the

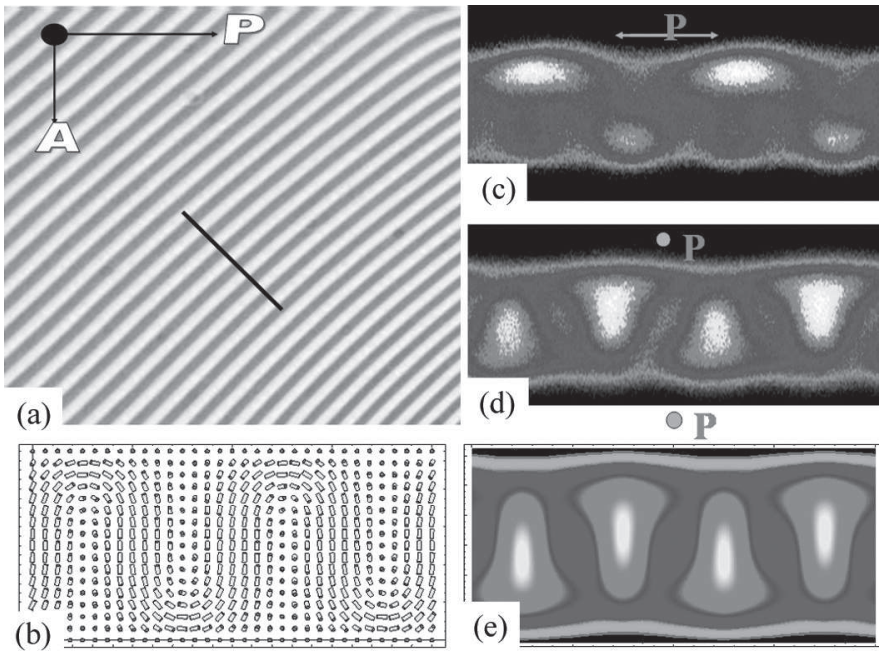

FIGURE 4 (a) Polarizing microscopy texture of a field-induced periodic structure in a thin cholesteric cell. (b) Computer-simulated director field in the cell's vertical cross-section. (c,d) Experimental vertical cross-sections of the structure for two orthogonal FCPM polarizations and (e) Computer-simulated FCPM texture corresponding to (d). For details on computer simulations of (b,e) see Refs. [7,8]. The fluorescence intensity color scale is the same as in Figure 2. The black line in (a) indicates the location of FCPM cross-sections (c,d).

experiment. Since the cell thickness and cholesteric pitch are of the same order as the spatial resolution, the features of FCPM textures are determined not only by $\hat{n}(\vec{r})$ and FCPM polarization, but also by effects of finite resolution [6,7]. For example, in the regions at bounding plates with $\hat{n}(\vec{r})$ parallel to $\widehat{P}$, the fluorescence signal does not drop to zero at the LC-substrate interface but is blurred over the distance determined by the resolution. The fluorescence signal in each pixel of the FCPM image is an integral of fluorescence intensity over a diffraction-limited volume determined by resolution: $I_{FCPM}(x,y,z) \propto \int\int\int I(x',y',z')T(x-x',y-y',z-z')dx'dy'dz'$, where T is the weight function that in simulations is assumed to be of the Gaussian type [7,8]. Therefore, the comparison of experimental FCPM textures with computer-simulated $\hat{n}(\vec{r})$ and textures accounting for the finite resolution (Fig. 4) is important to identify the director structures.

Once the basic features of a director structure are deciphered, it can be further studied, say, as a function of applied electric field. Figure 5 shows the FCPM vertical cross-sections of a cholesteric cell in the π-Grandjean zone for different applied voltages. Starting from the

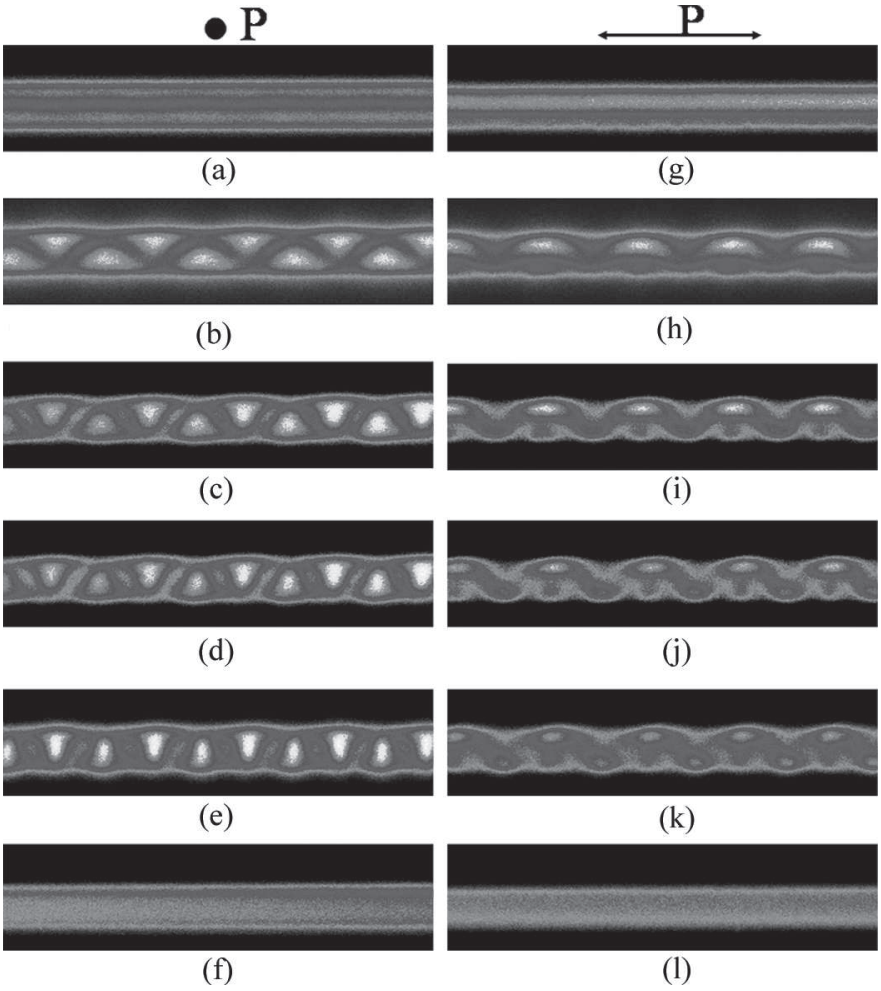

FIGURE 5 Vertical cross-sections of director structures in the π-Grandjean zone of a planar cholesteric cell for two orthogonal polarizations and at voltages: (a,g) U = 0; (b,h) U = 3 V; (c,i) U = 3.5 V; (d,j) U = 4 V; (e,k) 5 V; (f,l) U = 10 V.

threshold, $\hat{n}(\vec{r})$ continuously changes with voltage increase up to ~ 8 V at which a transition to a homeotropic texture takes place. At voltages > 8 V, $\hat{n}(\vec{r})$ is unwound and vertical everywhere but in the thin regions next to the substrates. This is visualized by the FCPM optical slice of Figure 5f,i in which the two stripes of somewhat stronger fluorescent signal next to the substrates correspond to the thin interfacial layers with in-plane $\hat{n}(\vec{r})$. The examples above demonstrate that (especially when used in conjunction with computer simulations) FCPM is capable to decipher 3-D director fields, even when the LC is confined into thin cells and director distortions have micrometer length-scales comparable to diffraction-limited resolution. The resolution effects have to be accounted for in the analysis of FCPM textures with micron-sized features.

3.2. Shape of Meniscus and Director Structures in Free-Standing Films

One of the fascinating properties of lamellar LCs is that they can form thin free-standing films [1,2]. Recently, the attention has been drawn to the meniscus region of free-standing SmA films [20,21], in which the film thickness usually changes in a broad range from nanometers to tens of micrometers [20]. To demonstrate how FCPM can be used for the director imaging in LC films of varying thickness, we use materials CCN-47 and 8CB (obtained from EM Chemicals), which exhibit the SmA phase at the room temperature. Free-standing films are suspended across 2 mm-wide holes drilled in either glass or metal supporting plates. The films are kept for several hours before the experiment in order to obtain stationary film profiles and the sample is equilibrated for (5–10) min after each temperature change. The temperature is controlled with accuracy ≈ 0.1 K. LCs are doped with ~ 0.01 Wt.% of two different fluorescent dyes (Fig. 2c,d), Nile Red and N-((2-(iodoacetoxy)ethyl)-N-methyl)amino-7-nitrobenz-2-oxa-1,3-diazole (IANBD ester), both purchased from Molecular Probes. The dyes homogeneously distribute within a thin LC film, Figure 6a. Anisotropic molecules of Nile Red, Figure 2c, align along $\hat{n}(\vec{r})$ so that the fluorescent signal from this dye allows one to determine the 3-D director field. The molecular shape of IANBD ester is different from that of LC molecules and the transition dipoles of this dye are disordered in the LC matrix; the fluorescence from IANBD ester is thus used to trace the film profile. Nile Red is excited by the Kr-laser and the fluorescent signal is detected in the spectral range 585–650 nm (channel #2). IANBD ester is excited by Ar-laser and fluorescence is detected in the range 510–550 nm (channel #1). The absorption and fluorescence bands of the dyes are well-separated and matched to the respective excitation and emission channels, as needed for the two-channel FCPM studies.

The thickness d is measured using the vertical cross-sections, Figure 6. Since the IANBD ester is not aligned by the LC host, its fluorescence directly visualizes the profile of the labeled film but only at thicknesses $d > 1\,\mu$m (because of the finite microscope's axial resolution). The meniscus profile (Fig. 6c, detection channel #2) can be fitted by the expected dependence $z = b \pm \sqrt{R^2 - (x-a)^2}$ [21] (see Fig. 6b), where R is the circle's radius and a, b determine its center's coordinates. The meniscus shape is circular up to film thickness 50 μm, but deviates from that in thicker parts of the film. The FCPM fluorescence from Nile Red (Fig. 6d) visualizes $\hat{n}(\vec{r})$. One can distinguish the following meniscus regions (Fig. 6) [21,22]: (1) central part of the film

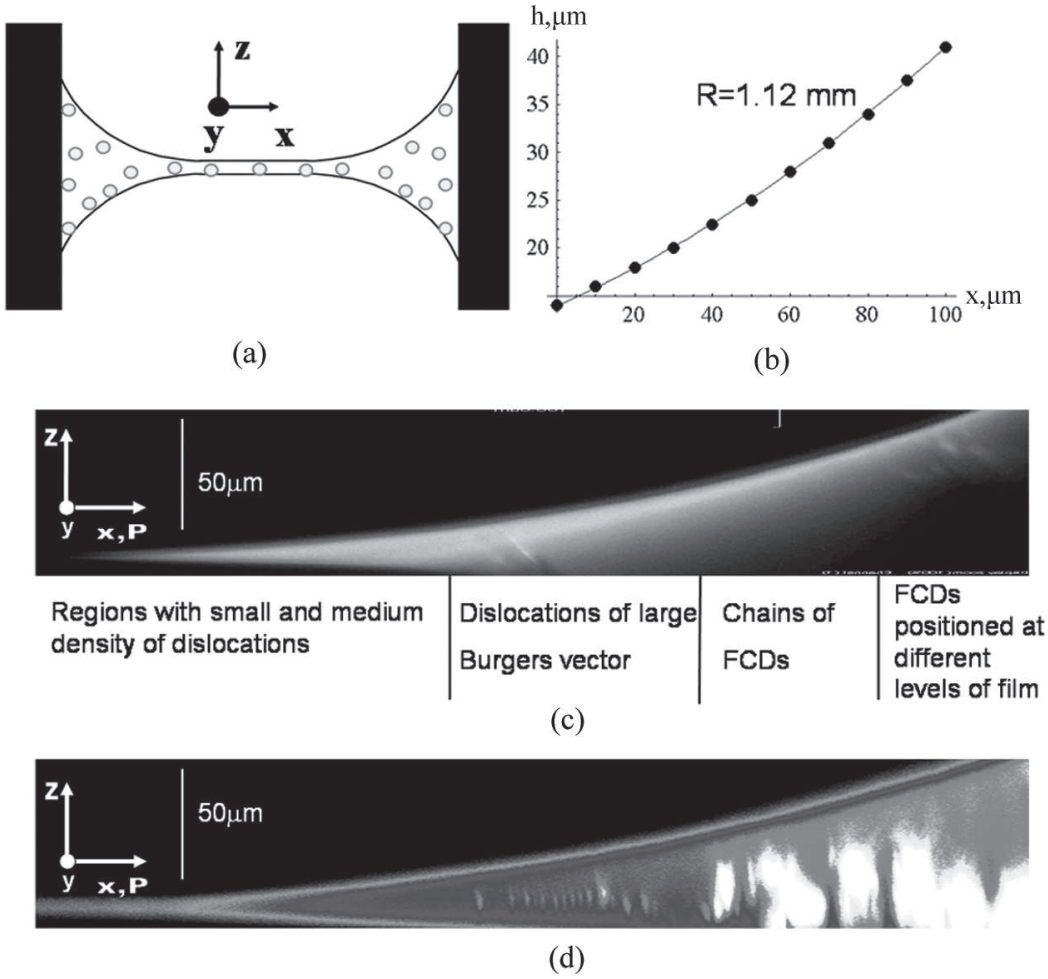

FIGURE 6 Meniscus region of a SmA free-standing film: (a) schematics of a dye-labeled free-standing smectic film supported by the rigid walls at the edges; (b) best fit of the experimental meniscus shape (dots) with the circular profile (solid line); (c) FCPM texture visualizing shape of meniscus (channel #1); (d) FCPM texture visualizing director distortions in the meniscus region of the film (channel #2).

with low dislocation density; (2) part with medium dislocation density; (3) region next to the supporting wall with dislocations of large Burgers vector and FCDs. In free-standing SmA films of thicknesses $(10-20)\mu$m, the dislocations of large Burgers vector often transform into chains of FCDs. Generally, size and eccentricity of FCDs increase with the film thickness as well as with the angle θ between the horizontal plane and the LC-air interface. The oily streaks of large Burgers vector are often replaced by several oily streaks of smaller Burgers vector, Figure 7. For M dislocations of Burgers vector b_j and N FCD ellipses with eccentricities e_i and the larger semiaxes a_i, the total Burgers vector is conserved, $b_t = \sum_j^M b_j + 2\sum_i^N a_i e_i = \text{const}$,

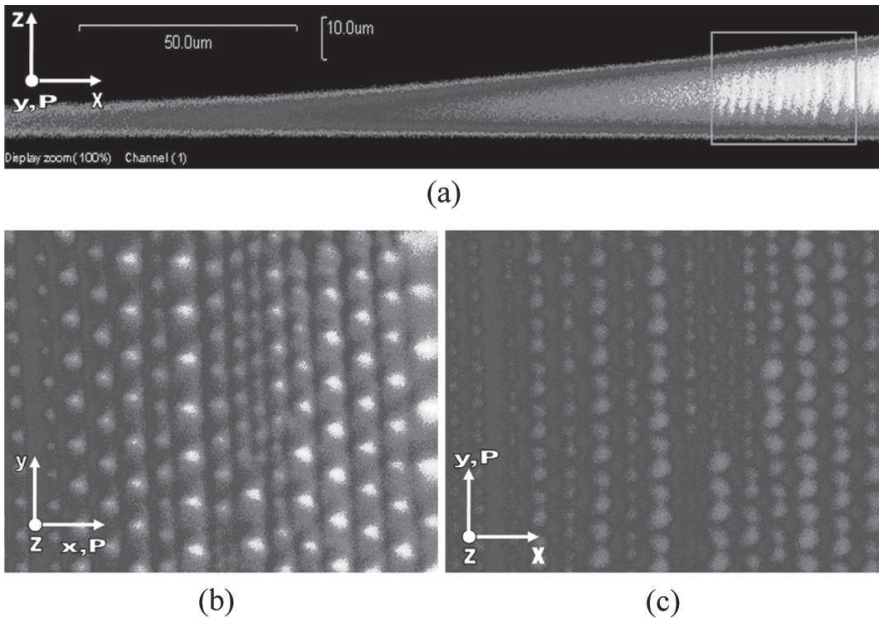

FIGURE 7 Chains of focal conic domains in the meniscus region of free-standing film as visualized by FCPM: (a) vertical xz-section; (b,c) xy-sections with the polarizer (b) along the thickness gradient (x-direction) and (c) perpendicular to the thickness gradient (along the y-direction).

Figure 7 [22]. Up to the thickness $(20-40)\mu m$, the elliptical FCD bases are located approximately in the middle plane of the film. This observation can be explained by the homeotropic anchoring at the LC-air interface which favors the locations of the elliptical bases in the film's middle plane (because the surface anchoring energy at air-LC interfaces is minimized). In the thicker parts of the films, the FCD elliptical bases are often displaced from the middle plane but always remain in the film bulk and rather far from the surfaces. The size of FCDs increases with film thickness within $(10-40)\mu m$. When the film thickness exceeds $(50-70)\mu m$, the FCDs can be located at different levels of the vertical cross-section, Figures 6,7. Thus, FCPM allows one to simultaneously study both LC film profiles and the respective director structures.

3.3. Colloidal Self-Organization in Liquid Crystals and Director Structures

Now we discuss the FCPM applications to LC emulsions and suspensions that show wealth of fascinating phenomena such as elasticity-mediated colloidal interactions [23]. We use colloidal system of glycerol droplets at the LC surface, Figure 8, obtained as in Ref. [15].

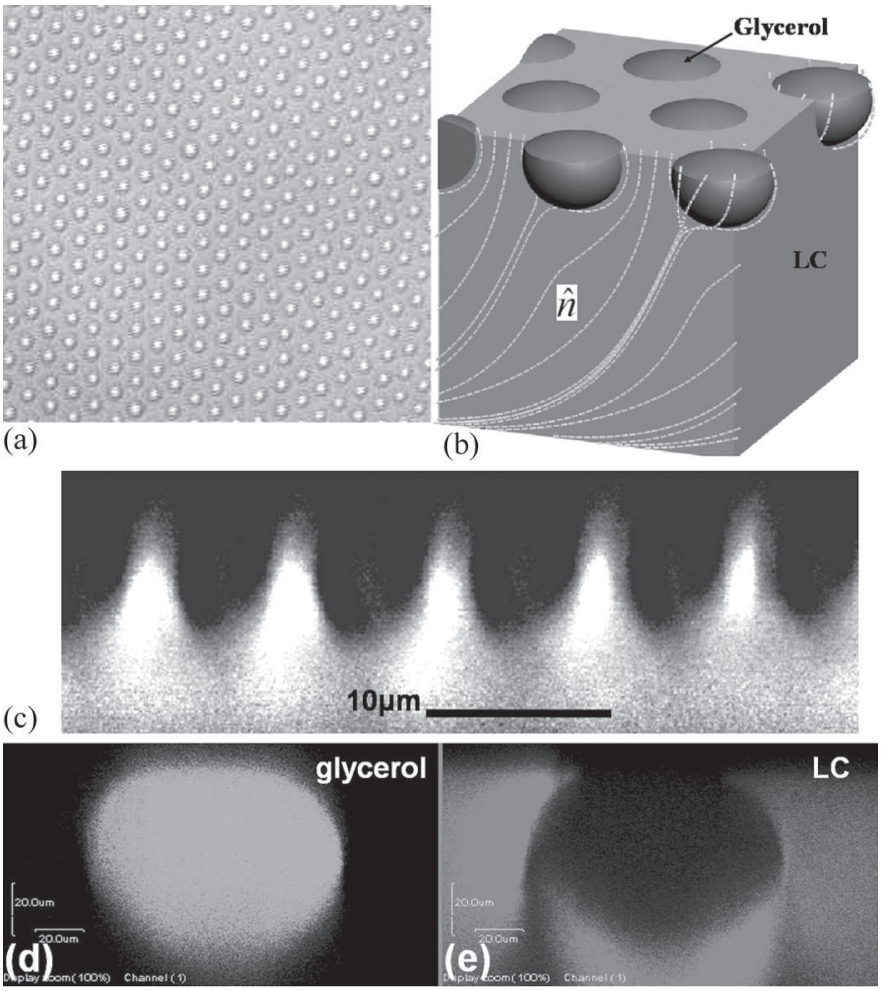

FIGURE 8 Hexagonal droplet array at the LC-air interface of a thick nematic film. (a) In-plane optical image. (b) Schematics of droplet positions and director field in the film. (c) FCPM vertical cross-section along a symmetry axis in the array. (d,e) Vertical cross-sections obtained with two-channel FCPM show: (e) the LC layer; (d) glycerol droplets at the LC-air interface (see Ref. 15 for details).

A nematic film of 5CB (pentylcyanobiphenyl, EM Industries) on top of glycerol is kept in a Petri dish at $\approx 50^{\circ}$C for ≈ 30 min to facilitate diffusion of the glycerol molecules into the 5CB layer, which is in the isotropic phase. When the sample is cooled down to the room temperature, the phase-separated glycerol droplets appear in the nematic film. The droplet size is controlled by varying the cooling rate and thermal cycling. One eventually obtains hexagonal structures of droplets of a practically constant radius in the films of controlled thickness $d = (5 - 100)\mu$m.

To decipher $\hat{n}(\vec{r})$ and droplet locations in the LC film, dyes fluorescein and Nile Red (Fig. 2) are doped in small quantities (0.01 wt %) to tag the glycerol and LC, respectively. Fluorescein molecules are relatively

polar; their solubility in glycerol is much better than in 5CB; after the glycerol-LC phase separation, the Fluorescein molecules stay in glycerol whose polar molecules contain the same hydroxyl groups as the dye. Nile Red molecules have hydrophobic tails and anisometric shapes, similar to the LC; therefore, this dye stays predominantly in the LC after the phase separation. Nile red molecules are well aligned by the LC matrix, as needed for the LC director imaging. The maximum absorption wavelength of Fluorescein matches the wavelength of Ar-Laser excitation, 488 nm, whereas the Nile Red dye is efficiently excited by Kr-Laser at wavelength 568 nm. The emission crosstalk between the two fluorophores is negligible, which allows one to separate the fluorescent signals from the dyes using interference filters. Fluorescence is detected in the spectral ranges 510–550 nm from Fluorescein and 585–650 nm from Nile Red.

FCPM textures of the sample's vertical cross-section, Figure 8, demonstrate that glycerol droplets are trapped at the LC-air interface; top droplet parts are protruding from the nematic film, Figure 8. The polarized fluorescence signal from Nile Red visualizes $\hat{n}(\vec{r})$ around the droplets, Figure 8 [15]. The 5CB film is in the so-called hybrid state, as $\hat{n}(\vec{r})$ is parallel to the LC-glycerol interface at the bottom and perpendicular to the air-LC interface at the top, Figure 8b. For a better clarity, the images in Figures 8d,e are taken for a relatively large droplet and a thick LC layer; smaller drops, Figure 8c, are also located at the interface and produce similar director distortions. Thus, the two-channel FCPM along with multiple dye labeling allows one to decipher both spatial positions of particles/droplets and the LC director structures in the composite LC systems.

3.4. FCPM Imaging of Dynamic Processes in Anisotropic Colloidal Systems

The above example of FCPM imaging in the LC emulsion corresponds to a stationary $\hat{n}(\vec{r})$ in a heterogeneous system. Another degree of complexity in the FCPM imaging is added if one studies dynamic processes. An example of the FCPM application for imaging of such a process is shown in Figure 9. We use LC material 8CB (EM Chemicals) which is in the SmA phase at the room temperature. The LC is doped with a small quantity of micro-spheres and with ≈ 0.01 wt.% of the BTBP (Fig. 2a), and then introduced into a cell with homeotropic boundary conditions at the confining electro-conductive substrates treated with lecithin. The micro-particles are treated with polyisoprene for tangential surface anchoring. When introduced into a SmA matrix with the uniform far-field director perpendicular to the

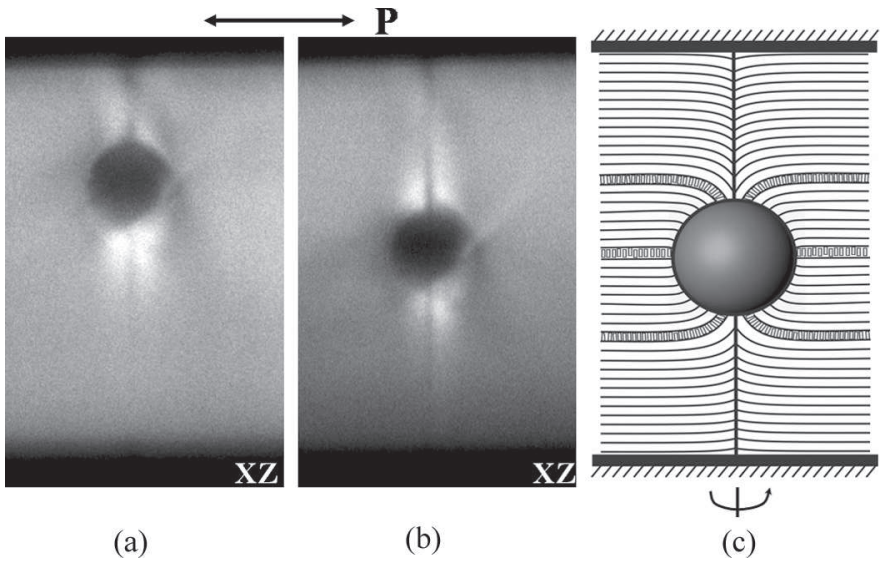

FIGURE 9 Elasticity- and anchoring-mediated colloidal particle levitation in middle of a cell with planar stack of smectic layers (homeotropic boundary conditions for the director at substrates): (a) after a particle has been shifted towards one of substrates by applying DC field $\sim 5\,\mathrm{V}/\mu\mathrm{m}$, (b) it returns back to the cell's middle plane to minimize the total bulk elastic and surface anchoring free energy. (c) Schematics of the layered structure and director around the bead.

bounding plates, the particles produce elastic distortions, Figure 9. The director structure is axially symmetric with respect to the axis orthogonal to the substrates and crossing the particle's center. By applying DC electric fields $\sim 5\,\mathrm{V}/\mu\mathrm{m}$, the particle can be shifted across the cell's vertical cross-section; the shift direction is determined by the voltage polarity. Using polarized FCPM signal from BTBP, we determine both $\hat{n}(\vec{r})$ and the particle positions in the cell, Figure 9. Figure 9a,b shows spatial displacements of particles in the vertical cross-section; the respective changes of $\hat{n}(\vec{r})$ are also visualized. A particle shifted towards one of substrates by electrostatic forces (due to applied voltage), Figure 9a, slowly returns back to the cell's middle plane after the field is switched off, Figure 9b. The reason for this particle levitation in the cell's middle plane becomes clear after considering the respective director structure, Figure 9c. The particle locations close to one of the substrates would imply strong deviations of the smectic layers from the orientation parallel to the cell substrates which is favored by the surface anchoring; the particle location at the cell's middle plane corresponds to minimum of these deviations. Thus, the surface anchoring and smectic elasticity mediate the particle levitation in the middle plane of the cell. Clearly, the gravity

forces acting on the micrometer-sized particle are negligible and the equilibrium particle's position is usually symmetric with respect to the bounding plates. Thus, FCPM allows one to explore dynamics in composite LC systems.

4. CONCLUSIONS AND OUTLOOK

We have demonstrated that Fluorescence Confocal Polarizing Microscopy allows one to image 3-D director fields not only in the spatially-homogeneous (in terms of composition) LCs, but also in the confined and composite LC materials. The technique also visualizes director structures changing in time, say, during particle motion in the LC. We show that using special dyes that mark different components of heterogeneous systems, one can get an access to the spatial 3-D patterns of both component distribution and director structures in LC emulsions and suspensions, confined and free-standing thin LC films, etc.

FCPM and several other techniques with optical 3-D resolution have been recently used to study molecular orientation patterns in the composite materials, including lyotropic LC systems and biological samples [24–40]. Certainly, the labeling-free techniques such as confocal Raman microscopy [39,40] and coherent anti-Stokes Raman scattering (CARS) microscopy [24,25] are of strong interest. However, the confocal Raman microscopy requires long-time signal integration or high laser powers [39,40] whereas the third harmonic generation (THG) [29,30], second harmonic generation [38], two photon fluorescence [34,35], and CARS microscopy techniques [24,25] employ nonlinear processes requiring sufficiently strong laser pulse energies necessary to ensure high conversion efficiency. These high laser powers may result in the realignment of the LC director [16] and even in the laser trapping of director structures caused by the optical gradient forces [17]. In fact, despite successful imaging of molecular orientations in complex biological, lyotropic, and thermotropic LC systems using some of these techniques [24–33], photodamage induced by the laser scanning of the structures such as myelin sheets has been also reported [32]. For example, the average laser powers used in CARS microscopy are usually (1–1000) mW, i.e., often strong enough to induce the director realignment in thermotropic nematic LCs confined into thick cells. One of the important advantages of using the FCPM is that the 3-D imaging of director structures in thermotropic LCs and the composite systems can be done using tiny laser excitation powers $\ll 1$ mW, at which both director realignment [16] and the influence of the optical gradient forces on the director structures [17] can be

neglected. Another advantage is that FCPM imaging of the composite systems can be background-free, which allows for a superior image contrast (unlike in the case of confocal Raman microscopy and the nonlinear microscopy techniques [24–40]). We conclude that the 3-D imaging of the director structures in composite materials using FCPM has a great potential for applications as a non-invasive high-contrast technique.

REFERENCES

[1] Chaikin, P. M. & Lubensky, T. C. (1995). *Principles of Condensed Matter Physics*, Cambridge University Press: Cambridge.

[2] de Gennes, P. G. & Prost, J. (1993). *The Physics of Liquid Crystals*, Clarendon Press: Oxford.

[3] Corle, T. R. & Kino, G. S. (1996). *Confocal Scanning Optical Microscopy and Related Imaging Systems*, Academic Press: San Diego.

[4] Sheppard, C. J. R. & Shotton, D. M. (1997). *Confocal Laser Scanning Microscopy*, BIOS Scientific Publishers: Oxford.

[5] Tanaami, T., Otsuki, S., Tomosada, N., Kosugi, Y., Shimizu, M., & Ishida, H. (2002). *Applied Optics*, *41*, 4704.

[6] Smalyukh, I. I., Shiyanovskii, S. V., & Lavrentovich, O. D. (2001). *Chem. Phys. Lett.*, *336*, 88.

[7] Shiyanovskii, S. V., Smalyukh, I. I., & Lavrentovich, O. D. (2001). In: *Defects in Liquid Crystals: Computer Simulations, Theory and Experiment*, Lavrentovich, O. D., Pasini, P., Zannoni, C., & Zumer, S. (Eds.). Chapter 10, Kluwer Academic Publishers: Amsterdam, 229; Smalyukh, I. I., Termine, D. J., Shiyanovskii, S. V., & Lavrentovich, O. D. (2001). *G.I.T. Imaging & Microscopy*, *3*, 16.

[8] Smalyukh, I. I. (2003). "Three-dimensional director fields studied by fluorescence confocal polarizing microscopy," Ph.D. Dissertation, Kent State University, Kent, OH, USA.

[9] Smalyukh, I. I. & Lavrentovich, O. D. (2002). *Phys. Rev. E*, *66*, 051703.

[10] Smalyukh, I. I. & Lavrentovich, O. D. (2003). *Phys. Rev. Let.*, *90*, 085503.

[11] Senyuk, B. I., Smalyukh, I. I., & Lavrentovich, O. D. (2005). *Opt. Lett.*, *30*, 349; Senyuk, B. I., Smalyukh, I. I., & Lavrentovich, O. D. (2006). *Phys. Rev. E*, *74*, 011712.

[12] Smalyukh, I. I., Kuzmin, A. N., Kachynskii, A. A., Prasad, P. N., & Lavrentovich, O. D. (2005). *Appl. Phys. Lett.*, *86*, 021913.

[13] Smalyukh, I. I., Senyuk, B. I., Shiyanovskii, S. V., Lavrentovich, O. D., Kuzmin, A. N., Kachynski, A. V., & Prasad, P. N. (2006). *Mol. Cryst. Liq. Cryst.*, *450*, 79.

[14] Smalyukh, I. I., Pratibha, R., Madhusudana, N. V., & Lavrentovich, O. D. (2005). *European Phys. J. E*, *16*, 179.

[15] Smalyuh, I. I., Chernyshuk, S., Lev, B. I., Nych, A., Ognysta, U., Nazarenko, V. G., & Lavrentovich, O. D. (2004). *Phys. Rev. Lett.*, *93*, 117801.

[16] Khoo, I.-C. (1995). *Liquid Crystals: Physical Properties and Nonlinear Optical Phenomena*, Wiley: New York.

[17] Smalyukh, I. I., Kaputa, D. S., Kachynski, A. V., Kuzmin, A. N., & Prasad, P. N. (2007). *Opt. Express*, *15*, 4359.

[18] Smalyukh, I. I., Senyuk, B. I., Gu, M., & Lavrentovich, O. D. (2005). *SPIE Procs.*, *5947*, 594707.

[19] Ford, W. E. & Kamat, P. V. (1987). *J. Phys. Chem.*, *91*, 6373.
[20] Pieranski, P. et al. (1993). *Physica A*, *194*, 364.
[21] Geminard, J. C., Holyst, R., & Oswald, P. (1997). *Phys. Rev. Lett.*, *78*, 1924.
[22] Boltenhagen, P., Lavrentovich, O. D., & Kleman, M. (1991). *J. Phys. II France*, *1*, 1233.
[23] Poulin, P., Stark, H., Lubensky, T., & Weitz, D. (1997). *Science*, *275*, 1770.
[24] Volkmer, A. (2005). *J. Phys. D: Appl. Phys.*, *38*, R59.
[25] Cheng, J.-X. & Xie, S. (2004). *J. Phys. Chem. B*, *108*, 827.
[26] Wang, H., Fu, Y., Zickmund, P., Shi, R., & Cheng, J.-X. (2005). *Biophys. J.*, *89*, 581.
[27] Kennedy, A. P., Sutcliffe, J., & Cheng, J.-X. (2005). *Langmuir*, *21*, 6478.
[28] Wurpel, G. W. H., Rinia, H. A., & Muller, M. (2005). *J. Microscopy*, *218*, 37.
[29] Pillai, R. S., Oh-e, M., Yokoyama, H., Brakenhoff, C. J., & Muller, M. (2006). *Opt. Express*, *14*, 12976.
[30] Oron, D., Tal, E., & Silberberg, Y. (2003). *Opt. Lett.*, *28*, 2315.
[31] Debarre, D. et al. (2006). *Nature Methods*, *3*, 47.
[32] Fu, Y., Wang, H., Shi, R., & Cheng, J.-X. (2006). *Opt. Express*, *14*, 3942.
[33] Kachynski, A. V., Kuzmin, A. N., Prasad, P. N., & Smalyukh, I. I. (2007). *Appl. Phys. Lett., 91*, 151905.
[34] Higgins, D. A. & Luther, B. J. (2003). *J. Chem. Phys.*, *119*, 3935.
[35] Xie, A. & Higgins, D. A. (2004). *Appl. Phys. Lett.*, *84*, 4014.
[36] Potma, I. O. & Xie, X. S. (2003). *J. Raman Spectrosc.*, *34*, 642.
[37] Cheng, J.-X., Pautot, S., Weitz, D. A., & Xie, X. S. (2003). *Proc. Nat. Acad. Sci. USA*, *100*, 9826; Muller, M. & Schins, J. M. (2002). *J. Phys. Chem. B*, *106*, 3715.
[38] Yoshiki, K., Hashimoto, M., & Araki, T. (2005). *Japanese J. Appl. Phys.*, *44*, 1066.
[39] Blach, J.-F., Warenghem, M., & Bormann, D. (2006). *Vibrational Spectroscopy*, *41*, 48.
[40] Ofuji, M., Takano, Y., Houkawa, Y., Takanishi, Y., Ishikawa, K., Takezoe, H., Mori, T., Goh, M., Guo, S., & Akagi, K. (2006). *Japanese J. Appl. Phys.*, *45*, 1710.